

Li–Zn Overlayer to Facilitate Uniform Lithium Deposition for Lithium Metal Batteries

Qiulin Chen, Hao Li, Melissa L. Meyerson, Rodrigo Rodriguez, Kenta Kawashima, Jason A. Weeks, Hohyun Sun, Qingshui Xie,* Jie Lin, Graeme Henkelman, Adam Heller, Dong-Liang Peng,* and C. Buddie Mullins*



Cite This: *ACS Appl. Mater. Interfaces* 2021, 13, 9985–9993



Read Online

ACCESS |



Metrics & More



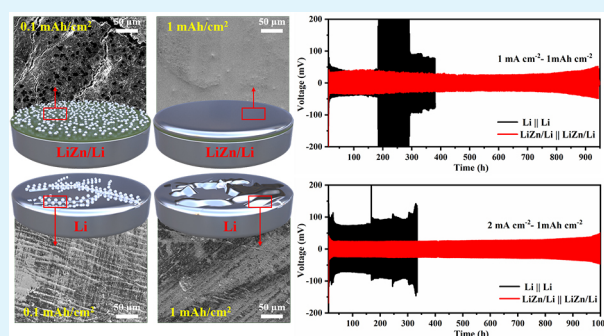
Article Recommendations



Supporting Information

ABSTRACT: The highly reactive nature and rough surface of Li foil can lead to the uncontrollable formation of Li dendrites when employed as an anode in a lithium metal battery. Thus, it could be of great practical utility to create uniform, electrochemically stable, and “lithiophilic” surfaces to realize homogeneous deposition of Li. Herein, a LiZn alloy layer is deposited on the surface of Li foil by e-beam evaporation. The idea is to introduce a uniform alloy surface to increase the active area and make use of the Zn sites to induce homogeneous nucleation of Li. The results show that the alloy film protected the Li metal anode, allowing for a longer cycling life with a lower deposition overpotential over a pure-Li metal anode in symmetric Li cells. Furthermore, full cells pairing the modified lithium anode with a LiFePO₄ cathode showed an incremental increase in Coulombic efficiency compared with pure-Li. The concept of using only an alloy modifying layer by an in-situ e-beam deposition synthesis method offers a potential method for enabling lithium metal anodes for next-generation lithium batteries.

KEYWORDS: Li metal anode, in-situ Li-alloy formation, alloy modifying layer, uniform nucleation and deposition, e-beam evaporation



1. INTRODUCTION

Lithium (Li) metal batteries are regarded as the most promising energy storage system for next-generation batteries because of their high energy density.^{1–4} As an anode material in Li battery systems, Li metal has been heavily studied due to its high theoretical capacity (3860 mAh g⁻¹), low working potential (–3.04 V vs the standard hydrogen electrode), and low density (0.534 g cm⁻³).^{5–7} However, the commercialization of Li metal batteries has been hindered for several important reasons. For example, the uneven deposition of Li contributes to the formation of dendrites, which leads to the formation of “dead Li”, low Coulombic efficiency (CE), high impedance, and even safety hazards.^{8–10} Additionally, the highly reactive nature of Li metal brings about severe side reactions between Li and ester-based electrolytes, which causes an accumulation of solid electrolyte interface (SEI) layers and losses in capacity.¹¹

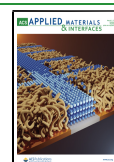
Several strategies have been proposed to realize homogeneous deposition of Li metal and formation of stable SEI layers, including electrolyte optimization, surface decoration, and construction of stable hosts.^{12–16} Meanwhile, the basic mechanisms at play in Li deposition remain an active area of research for battery science investigators,¹⁷ especially the initial nucleation and deposition of Li, which plays an important role in the sequential deposition and stripping of Li. Many models

have been suggested to understand the mechanism of initial deposition of Li. According to the heterogeneous nucleation model, to realize even deposition of Li, the wettability of the substrate plays an important role.^{18,19} Cui and co-workers explored the nucleation pattern of Li metal on different substrates (Au, Ag, Zn, etc.), and their results suggested that substrates with solubility to Li metal showed no nucleation barriers, indicating it is easier for Li to deposit on those substrates.^{20,21} More and more “lithiophilic” materials (CuO, Al₂O₃, Au, and Sn) have been reported to reduce the overpotential of Li during nucleation. For example, Shi and co-workers reported that the lithiophilic AuLi₃ particles on Ni foam skeletons can significantly lower the nucleation energy barrier and enhance the uniformity for Li deposition compared with single Ni foam.^{22–28} Matsuda and co-workers reported that the electrolytes which contain metal ions (Sn⁴⁺, Al³⁺, In³⁺, Ga³⁺, or Bi³⁺) would benefit the increase in Coulombic

Received: November 30, 2020

Accepted: February 8, 2021

Published: February 16, 2021



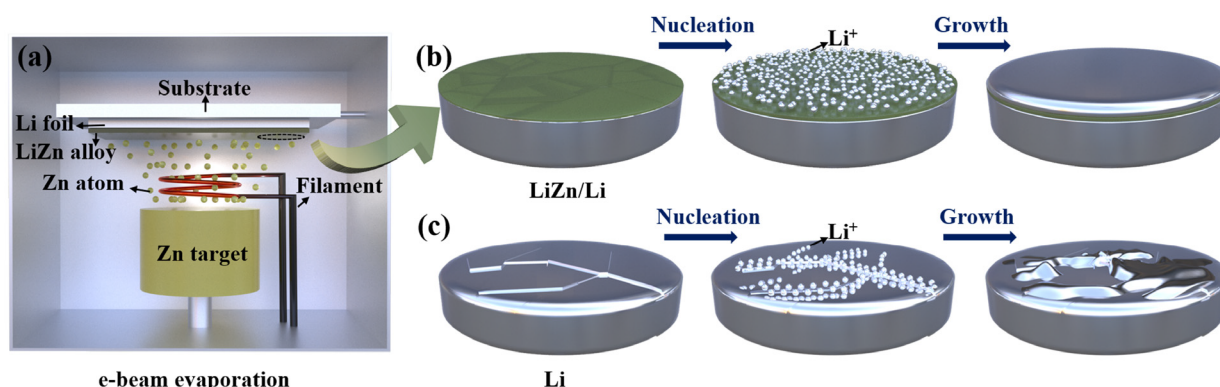


Figure 1. Schematic diagrams for (a) the synthesis of a LiZn alloy layer on the Li foil surface; the deposition behavior of Li ions on the surfaces of (b) the LiZn alloy modified Li foil and (c) pure-Li foil.

efficiency since the metal ions in the electrolyte would electrochemically form a Li-based alloy thin film on the surface of the Li substrate, which would increase the surface uniformity.^{29,30} Ye and co-workers reported a three-dimensional Cu current collector modified with Al (Cu@Al) as to make use of the reaction between Li and Al to generate a binary LiAl alloy phase in the first cycle.¹¹ The alloy is utilized to facilitate uniform metallic Li nucleation and growth. Constructing a stable “lithiophilic” surface would be effective in realizing homogeneous deposition of Li, forming a stable SEI layer, and increasing the CE. However, when pure metal (such as Al, Ag, Au, etc.) is used directly as an anode current collector in full cells, the initial CE will be low due to the alloying process in the initial cycle. Thus, it is of great utility to introduce an alloy modification layer via a facile method instead of employing a pure “lithiophilic” metal as the current collector.

Herein, a LiZn alloy overlayer is in situ introduced on a pure-Li surface by e-beam evaporation, as illustrated in Figure 1a, the purpose of which is to introduce a uniform alloy surface so that homogeneous deposition of Li metal can be realized. For the surface of a pure-Li foil (as shown in Figure 1b) is not ideal, it is much easier for Li^+ to accumulate at “hot spot” sites (like valley and edge sites) with a high surface free energy and high local current density and then nucleate and grow uncontrollably, which ultimately leads to the formation of lithium dendrites after repeated charging/discharging.³¹ By introduction of a LiZn alloy on the Li surface, the Zn sites in the alloy have higher solubility for Li, which can reduce the nucleation overpotential and increase the concentration of active sites, thereby reducing the local current density and realizing uniform nucleation of Li metal, as illustrated in Figure 1c. Additionally, the introduction of an electrochemically inert alloy layer can also assist in the reduction of the side reactions occurring on the surface of the Li metal, which would increase the CE of the system. What is more, the stability of the SEI layer on the surface of alloy can be improved greatly, for the structure of the introduced alloy layer is more stable when compared with pure-Li, which suffers from a large volume change during plating and stripping.

2. EXPERIMENTAL SECTION

2.1. Materials Preparation. The LiZn modified Li foil is in situ prepared by e-beam evaporation. Monocrystalline Zn pellets (purity 99.99%) contained in a crucible are evaporated onto the surface of the Li foil (with 99.9% purity and 0.75 mm thickness, Alfa Aesar, CAS#

7439-93-2). Before evaporation, the vacuum chamber is evacuated to a pressure lower than 10^{-8} Torr. Then, Li foil is transferred through an intermediate chamber into the stainless-steel chamber. Zn is deposited with a constant evaporator emission current of 0.2 mA. According to the phase diagram of Li–Zn, it is very facile to form a LiZn alloy with a large amount of Li. The deposition rate is around 0.5 \AA s^{-1} as measured by a quartz crystal microbalance.

2.2. Morphology and Structure Characterization. The morphologies of the samples were analyzed by a FEI Quanta 650 scanning electron microscope (SEM). Energy dispersive spectroscopy (EDS, Hitachi S5500) was used to observe the elemental dispersion in the cross section. The cross section of the electrodes is examined by using a Thermo Fisher Scientific Scios 2 HiVac dual-beam system with EBL capabilities (Scios Duslbeam), and the stage tilt was set to 45° when taking the images. X-ray powder diffraction (XRD) patterns of the samples were recorded on a Rigaku Ultima IV X-ray diffraction system with $\text{Cu K}\alpha_1$ radiation (40 kV, 30 mA) with a scan rate of $10^\circ \text{ min}^{-1}$. X-ray photoelectron spectra (XPS) were obtained by a Kratos Axis Ultra X-ray photoelectron spectrometer, with a monochromatic $\text{Al K}\alpha$ X-ray source ($h\nu = 1486.5 \text{ eV}$). Samples were transferred from an Ar-filled glovebox by using a transfer capsule. The data were analyzed by using Casa XPS software, and the peak binding energies were normalized to the adventitious C 1s peak aligned to 284.8 eV. Samples were sputtered with Ar^+ to obtain depth profiles.

2.3. Electrochemical Properties Investigation. The Li storage properties of the achieved products were tested by assembling 2032 coin-type cells in an argon-filled glovebox (water and oxygen levels $<0.1 \text{ ppm}$). The Li foil samples with evaporative-deposited Zn were used as the working electrode directly. A lithium metal disk and Celgard 2300 served as the counter electrode and the separator, respectively. We used 1 M lithium bis(fluorosulfonyl)imide (LiFSI) in dimethoxyethane (DME) as the electrolyte. For full cells, commercial FeLiPO_4 (LFP) was used as the cathode, and Li foils (with/without the LiZn modification) were employed as anodes. The cycling and rate performances of the cells were performed with an Arbin BT-2143 multichannel battery testing system. The electrochemical impedance spectroscopy (EIS) of the cells after different cycles were tested in the frequency range from 0.1 Hz to 2000000 kHz with an open-circuit voltage of 10 mV by using a Gamry Interface 1010E.

2.4. Computational Methods. All the density functional theory (DFT) calculations were performed with the VASP package. The electronic exchange and correlation were described by a generalized gradient approximation method using the Perdew–Burke–Ernzerhof functional.³² The core electrons were described by the projector augmented-wave method.³³ The valence electrons were described by Kohn–Sham wave functions expanded in a plane-wave basis;³⁴ the energy cutoff for the calculations was set to 400 eV. The Brillouin zone was sampled by a $3 \times 3 \times 1$ k -point mesh using a Monkhorst–Pack method.³⁴ Structures were considered optimized after all the forces fell below 0.05 eV/\AA .

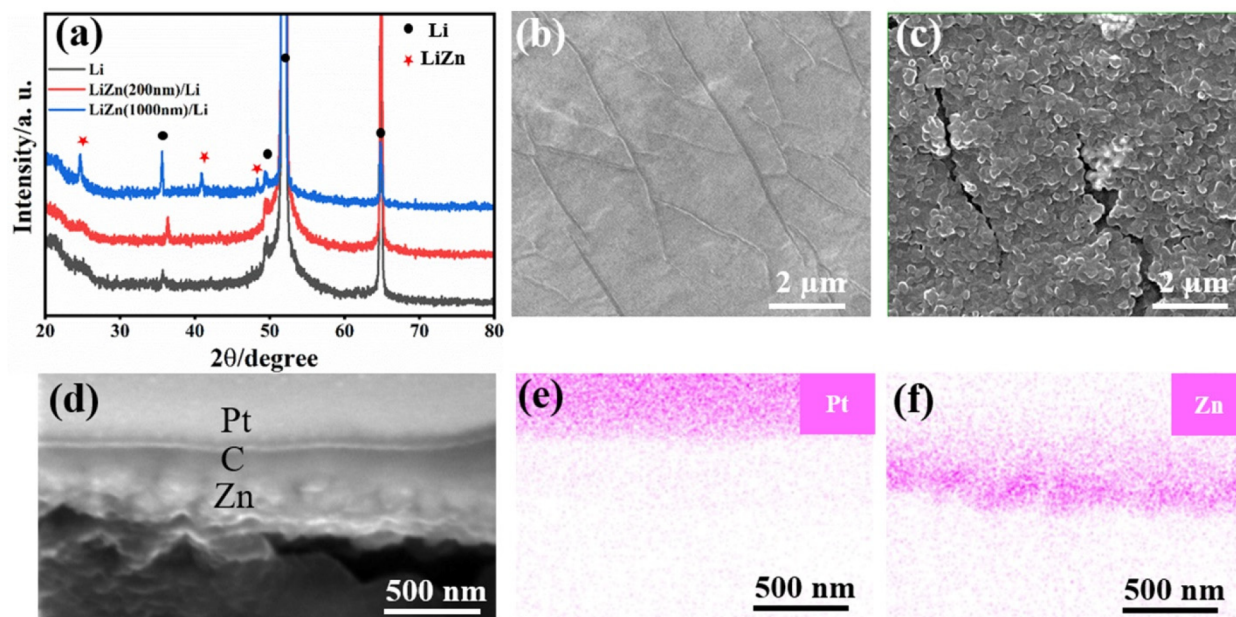


Figure 2. (a) XRD patterns of Li and LiZn/Li. SEM images of (b) pure-Li and (c) LiZn (200 nm) on Li. (d) FIB-SEM images of the cross-sectional view of LiZn (200 nm)/Li. EDS mapping of (e) Pt and (f) Zn elements.

The Li and LiZn surfaces were modeled as four-layer, 4×4 slabs. All slab surfaces were cleaved from the bulk structures with DFT-optimized lattice constants. The surface energies (E_{surf}) were calculated via eq 1:

$$E_{\text{surf}} = \frac{E_{\text{slab}} - nE_{\text{bulk}}}{2A} \quad (1)$$

where E_{slab} and E_{bulk} are the total energies of the slab surface and the bulk structure, respectively, n is the ratio of the atoms in the slab with the bulk, and A represents the area of the unit cell. The binding energies of Li (E_{b}) are calculated by using eq 2:

$$E_{\text{b}} = E_{\text{Li}^*} - E_{\text{slab}} - E_{\text{Li}} \quad (2)$$

where E_{Li^*} is the total energy of a surface with an adsorbed Li atom and E_{Li} is the total energy of a Li atom in a vacuum calculated with spin polarization.

3. RESULTS AND DISCUSSION

3.1. Morphology and Structure Analysis. The XRD patterns of pure-Li and LiZn alloy modified Li are displayed in Figure 2a. The characteristic peaks of Li and LiZn (thickness: ~ 200 nm)/Li can be identified to Li (PDF 00-015-0401). No LiZn alloy peak can be detected in LiZn (200 nm)/Li, which can be attributed to the low mass loading of the alloy. After increasing the thickness of the LiZn alloy layer to 1000 nm, the diffraction peaks for the LiZn alloy appear (PDF#03-065-4082). The SEM image of the top surface for pure-Li foil is shown in Figure 2b; it can be found that the surface is not even, with lots of “gullies” spreading out over the entire surface, which can serve as “hot spots” for the accumulation and nucleation of Li^+ ions during cycling. The top surface morphology of LiZn/Li is displayed in Figure 2c. Compared with pure-Li, LiZn/Li shows higher surface roughness due to the introduction of the LiZn particle film, which can help to reduce the local current density and provide more nucleation sites in the deposition of Li metal. One can find that cracks exist on the surface of the LiZn alloy, which might be attributed to the original rough Li surface, for the width between the cracks is the same as that on pure-Li foil.

However, the cracks almost have no effect on the nucleation behavior of Li metal on the LiZn alloy surface, which will be confirmed later. It was found that the alloy particles are well distributed on the Li surface. Figure S1a,b shows the Zn particles on the Si substrate, the size of which ranges from 50 to 300 nm. Because Zn particles would not react with the Si substrate, the Zn atoms would first nucleate on the Si substrate, and the Zn atoms from different angles have different kinetic energies; thus, Zn crystals with different sizes would be formed on the surface of the Si substrate and show hexagonal morphology. Alternatively, Zn atoms would react with Li metal to form a LiZn alloy layer when Zn atoms reach the Li surface. The alloying process would change the morphology of the deposited “Zn” (LiZn) layer on the Li foil due to its different microstructure and composition compared to the deposited Zn particles on the Si substrate. A cross-sectional FIB-SEM image of LiZn/Li is exhibited in Figure 2d. The top Pt layer is introduced to protect the alloy layer during FIB sputtering. Figure 2e,f presents the EDS mappings of Pt and Zn elements. It was found that the modifying alloy layer is uniform and compact with a thickness of around 200 nm.

Figure S2 presents the Li 1s, C 1s, O 1s, and Zn 2p XPS depth profiles of LiZn/Li. The detailed XPS spectra of Li 1s are shown in Figure S2a, and the peaks located at 58.0, 56.2, and 55.0 eV can be attributed to Li_2CO_3 (or LiOH), Li_2O , and Li metal. It can be found that the peaks shift to lower binding energy, showing a more metallic nature for Li with increases in sputtering time.³⁵ Such a phenomenon can be ascribed to the native oxide layer on the Li metal surface, which can be confirmed by the decrease in C 1s and O 1s XPS spectra with increasing of the sputtering time (shown in Figure S2b,c). Two major peaks centered at 1022.6 and 1045.7 eV with a spin-energy separation of 23.1 eV correspond to Zn $2p_{3/2}$ and Zn $2p_{1/2}$ for Zn^{2+} in Figure S2d.³⁶ The Zn 2p XPS spectra also show more metallic nature with increases in sputtering time, which is similar to Li 1s.

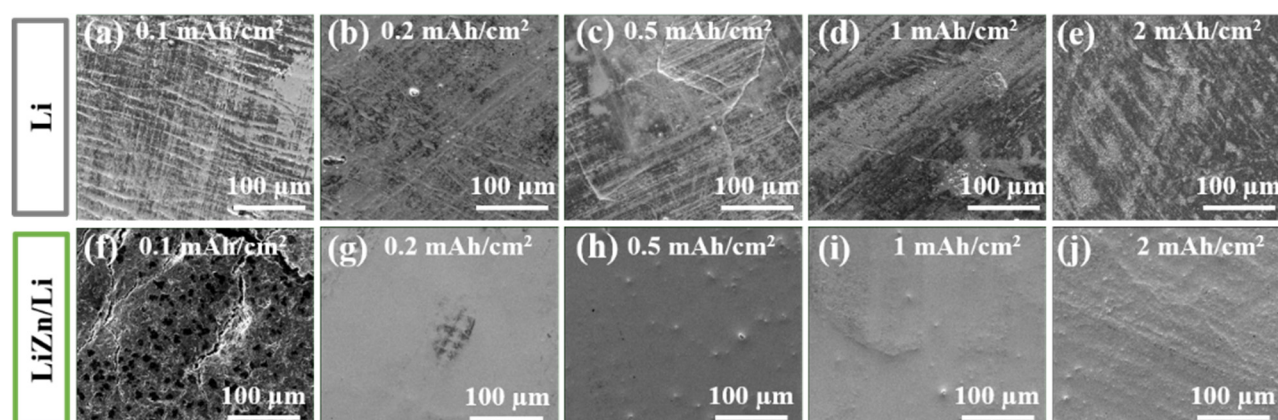


Figure 3. SEM images of the surface of Li foil with deposition of Li at 2 mA cm⁻² for (a) 0.1, (b) 0.2, (c) 0.5, (d) 1, and (e) 2 mA h cm⁻². SEM images of the surface of LiZn/Li with deposition of Li at 2 mA cm⁻² for (f) 0.1, (g) 0.2, (h) 0.5, (i) 1, and (j) 2 mA h cm⁻².

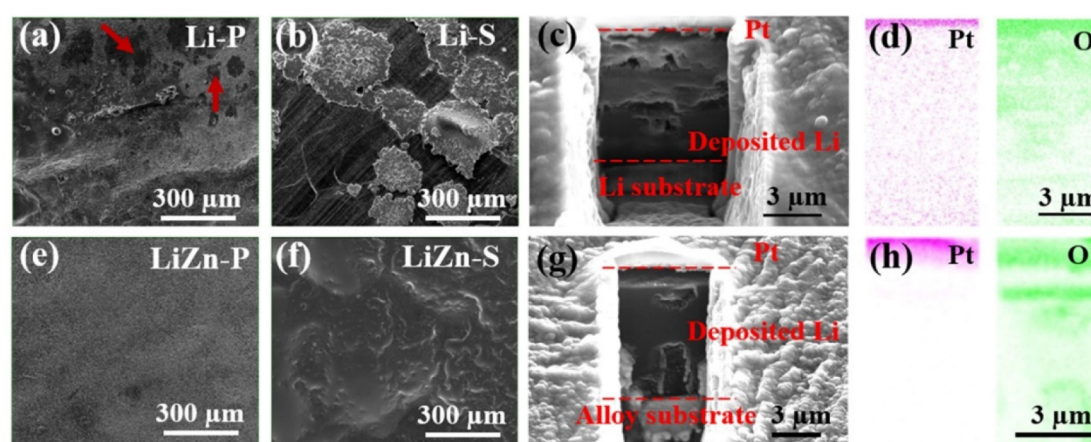


Figure 4. SEM images of Li surface: (a) Li plating side and (b) Li stripping side. (c) Cross-sectional FIB-SEM images of plating sides of Li. (d) EDS mappings of Pt and O elements. SEM images of LiZn/Li surface: (e) Li plating sides and (f) Li stripping sides, after 100 cycles at a current density of 2 mA cm⁻² for 2 mA h cm⁻². (g) Cross-sectional FIB-SEM images of plating sides of LiZn/Li. (h) EDS mappings of Pt and O elements.

To find a suitable modification thickness for the LiZn alloy layer, different quantities of Zn (100, 200, and 400 nm) were evaporated onto the surface of the Li foil. After that, 2 mA h cm⁻² of Li is deposited on the surface of the modified Li (with different thicknesses of alloy layers) at a current density of 2 mA cm⁻²; the corresponding SEM images are shown in Figure S3. It can be found that the deposition of Li on LiZn (100 nm)/Li is not as uniform as those on LiZn (200 nm)/Li and LiZn (400 nm)/Li. The reason can be ascribed to the low mass loading of Zn particles, leaving some inactive areas. After increasing the amount of evaporated Zn, the surface of the Li foil is fully covered; thus, the active area increases, and the deposition of Li becomes more uniform. In the following discussion, the thickness of Zn layer was chosen to be 200 nm.

Because the initial nucleation of Li metal plays an important role in the subsequent growth of Li, different amounts of Li are deposited on the different surfaces to explore the initial nucleation and deposition behaviors. After the deposition of 0.1 mA h cm⁻² of Li on a pure-Li surface, most of the Li metal nucleates in the “gully” portions (brighter sites), and only part of the surface is used, as shown in Figure 3a. The deposition of Li is nonuniform after the deposition amount increases to 2 mA h cm⁻² (shown in Figure 3b–e). The reason for such a phenomenon can be attributed to the “gully” portions having a higher surface free energy and current density.^{37,38} However,

after the introduction of the LiZn alloy layer, the nucleation behavior of Li is much different from that on a pure-Li surface. It can be seen that the nucleation sites of Li metal on the LiZn alloy surface are not along the “gully” but well distributed (Figure 3f) on the surface, indicating that LiZn alloy surface is more “lithiophilic” than that of a “gully” area. Additionally, the deposition of Li on the alloy surface remains uniform, even when the deposition capacity increases to 2 mA h cm⁻². The comparison of Li deposition behaviors between the pure-Li surface and the LiZn alloy surface proves that the LiZn alloy surface can not only benefit the nucleation of Li but also increase the active area to achieve homogeneous Li deposition. Zoomed-in pictures have been added in Figure S4 accordingly. One can find that the deposition behavior of the Li metal on the pure-Li foil is mainly along the “gully”, while the nucleation of Li on the surface of the LiZn alloy is well distributed. As the deposited amount of Li is gradually increased, the LiZn alloy surface is smoother than those of the pure-Li foil surface.

After 100 cycles at a current density of 2 mA cm⁻² for 2 mA h cm⁻², the plating side of Li (Li-P) shows a porous structure (Figure S5a), and there are still inactive sites remaining (marked in red arrow, in Figure 4a), indicating a low surface area is involved in plating/stripping and nonuniform Li deposition. Additionally, the EDS mapping of F on the Li surface, which originates from the formed SEI layer, is also

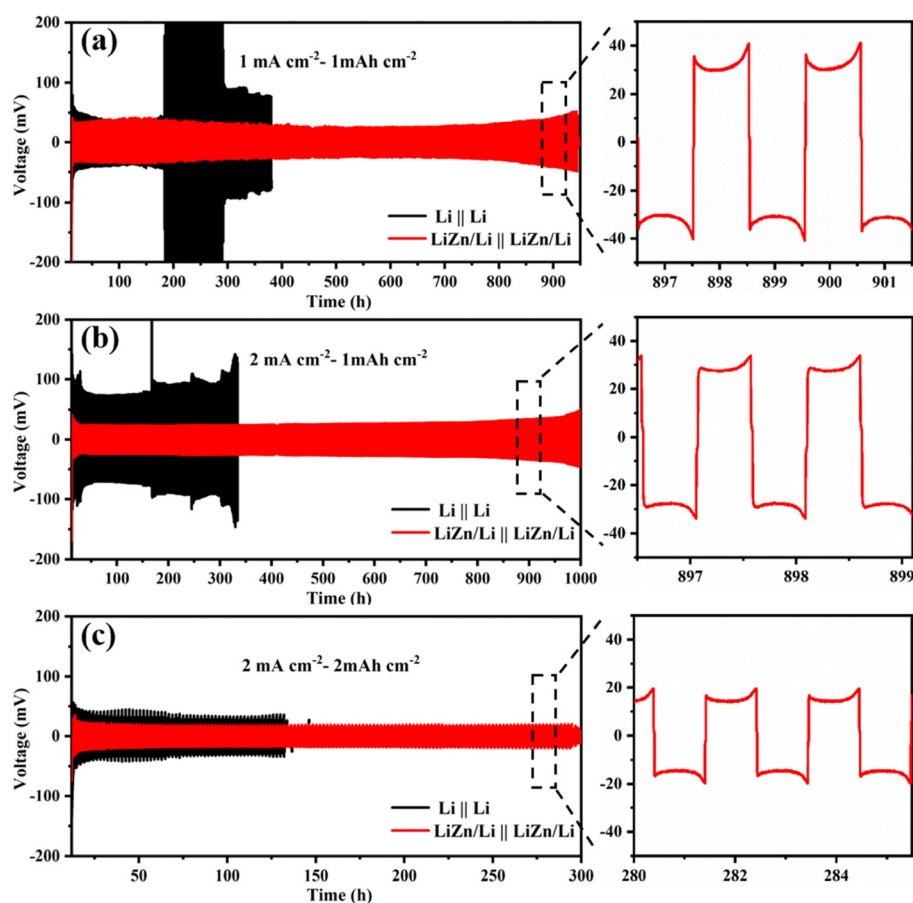


Figure 5. Comparisons of the cycling stability of Li||Li and LiZn/Li||LiZn/Li symmetric cells at a current density of (a) 1 mA cm^{-2} for a total capacity of 1 mAh cm^{-2} and (b) 2 mA cm^{-2} for 1 mAh cm^{-2} , and (c) 2 mA cm^{-2} for 2 mAh cm^{-2} .

distributed unevenly, as shown in Figure S5b. Such a phenomenon can be attributed to the various surface formation energies and diffusion barriers of the species on the surface, leading to the uneven stripping/plating of Li and further causing uneven formation of the SEI.¹⁸ When it comes to the stripping side of Li (Li-S), it can be seen that the surface is covered with a porous structure (Figure S5c), and a large number of “dead” Li or side products are formed (Figure 4b). However, compared with the Li surface, the deposition of Li on the plating side of the LiZn alloy surface (LiZn-P) is much more homogeneous and denser (Figure S5d,e), and the deposited Li is well covered on the top surface to reveal no inactive surface areas. In addition, the EDS mapping of F on the LiZn alloy surface is well distributed, as shown in Figure S5e. For the stripping side of the LiZn alloy surface (LiZn-S), no apparent porous structure can be seen (Figure 4f), and almost no “dead” Li is left on the surface (Figure S5f). The cross-sectional FIB-SEM image of the plating sides of Li after 100 cycles in Figure 4c shows that the deposition of Li is porous on the Li metal surface. The uneven deposition of Li on the pure-Li foil leads to the formation of Li dendrites and then new SEI layers due to the side reactions between Li dendrites and electrolyte. After repeated deposition and dissolution, the deposited Li dendrites covered by SEI layer will form a porous layer on the surface of the pure-Li foil, leading to a wide distribution of SEI layers in thickness, as indicated in the distribution of O in the EDS mapping shown in Figure 4d. However, the top surface of the LiZn/Li surface is flat, and no apparent porous structure can be seen in Figure 4g. According

to the distribution of O in Figure 4h, the distribution of the SEI is relatively narrow compared with pure-Li, which can be ascribed to the better structural stability of the alloy layer. The gap between O and Pt (Figure 4h) is caused by the exfoliation of the Pt layer from the top surface of the Li metal during the FIB cutting process.

3.2. Electrochemical Performance Measurement. The voltage profiles for Li||Li and LiZn/Li||LiZn/Li symmetric cells at a current density of 1 mA cm^{-2} for a total capacity of 1 mAh cm^{-2} are shown in Figure 5a. The nucleation overpotential is defined as the gap between the dip voltage and the stable voltage plateau.³⁹ It can be seen that the nucleation overpotential for the LiZn/Li||LiZn/Li symmetric cell (22 mV) is lower than that for the pure-Li||Li symmetric cell (34 mV) due to the high solubility of Zn in the LiZn alloy with Li and the increased surface area.⁴⁰ In addition, we find that the shape of these two curves are also different. The existence of an arc in the voltage profile (the circled parts in Figure S6) in earlier cycles indicates that a large surface variation exists on the pure-Li surface.⁴¹ The fluctuations in the voltage profile of the Li||Li symmetric cell (Figure S6) can be attributed to the formation of the unstable SEI layer on the Li foil due to uneven Li deposition and the resultant large impedance in the following cycles. The pure-Li||Li symmetric cell shows a cycling life of 180 h before it shows abrupt polarization. However, the LiZn/Li||LiZn/Li symmetric cell shows a longer cycling life of around 950 h. When the current density increases to 2 mA cm^{-2} , the LiZn/Li||LiZn/Li symmetric cell still shows superior cycling life over the pure-Li||Li symmetric cell (Figure 5b). The

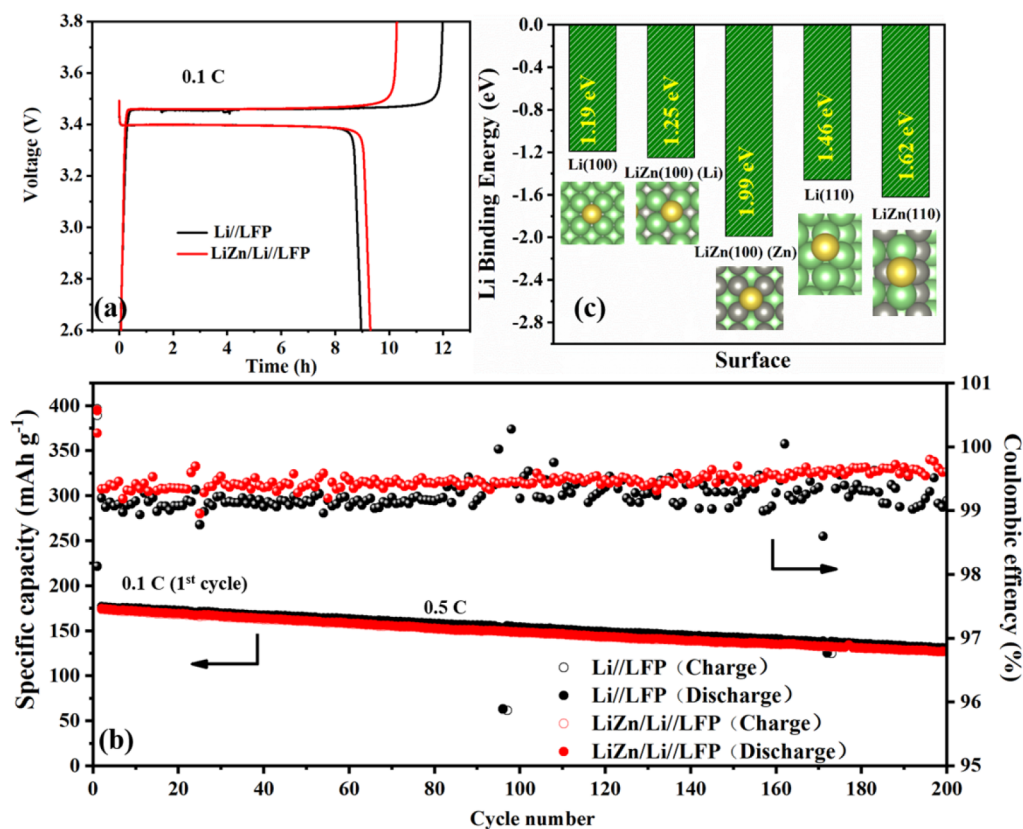


Figure 6. (a) Voltage profiles and (b) cycling performance of Li//LFP and LiZn/Li//LFP full cells and calculated binding energies of Li on five surfaces (c). Both the Li and Zn terminations on LiZn (as indicated in the brackets) were considered on the calculations on the (100) surface.

deposition overpotential almost does not change when the deposition amount increases to 2 mAh cm⁻² (as shown in Figure 5c) due to the optimized local current density which relates to the increase in active area. Li||Li symmetric cells show serious polarization and an obvious increment in the deposition overpotential due to the drastic changes in the structure and the electrode materials on the Li surface caused by the rapid migration of Li⁺ ions and redox reactions on the pure-Li surface.^{18,42} The LiZn/Li||LiZn/Li symmetric cells present a cycling life of around 300 h at current densities of 2 for a total capacity of 2 mAh cm⁻² (Figure 5c), indicating that the LiZn/Li electrode shows promising stability, and the exact zoomed-in voltage profiles of hundreds of cycles are added in Figure 5a–c to exclude possible short circuits. One can find that all the voltage profiles show a steady voltage plateau with a relatively low overpotential. Figure S7 shows the EIS plots and the equivalent circuit for the pure-Li||Li and LiZn/Li||LiZn/Li symmetric cells at a current density of 2 mA cm⁻² for a total capacity of 1 mAh cm⁻² before and after one cycle. It can be found that both plots show a semicircle in the high-frequency region, and the diameter of which can be regarded as the charge transfer impedance (R_{ct}) on the surface of the SEI and the surface of the electrode. Clearly, the circle diameter for the LiZn/Li||LiZn/Li symmetric cell is much lower than that of the pure-Li||Li symmetric cell, indicating fast charge transfer on the surface of LiZn/Li||LiZn/Li which can be attributed to the larger active surface area. Both R_{ct} values decrease after one cycle, which can be attributed to further increases in surface area after deposition of Li.⁴³

To explore the potential practical application of the LiZn/Li anode, we fabricated full cells using LiFePO₄ (LFP) as the

cathode. The voltage profiles of two full cells in the voltage window of 2.5–3.8 V at a current density of 0.1 C (1 C = 170 mA g⁻¹) during the first cycle are displayed in Figure 6a. Typical discharge plateaus for LFP at around 3.4 V vs Li⁺/Li are observed in both Li//LFP and LiZn/Li//LFP full cells. The pure-Li//LFP full cell shows a higher specific charge capacity and lower specific discharge capacity than that of the LiZn/Li//LFP full cell in the first cycle, indicating more side reactions, and irreversible consumption of Li⁺ ions takes place on the pure-Li surface. In contrast, the LiZn/Li//LFP full cell shows a higher discharge capacity and reversibility compared with the pure-Li//LFP full cell. Figure 6b exhibits the cycling performance of pure-Li//LFP and LiZn/Li//LFP full cells at 0.5 C. The two full cells show nearly the same specific capacity (around 130 mAh g⁻¹) after 200 cycles. The CEs of the LiZn/Li//LFP full cell are higher than that of a Li//LFP full cell, which can be attributed to more uniform deposition of Li on the surface of the LiZn alloy due to its good lithiophilic features, so that fewer side reactions happen. Additionally, one can find that the CEs of the Li//LFP full cell shows larger fluctuations than the LiZn/Li//LFP counterpart, and the CEs even exceed 100% every now and then, indicating the formation of Li dendrites on the surface of the pure-Li surface. Both are responsible for the lower CEs of the Li//LFP full cell.

To evaluate the nucleation and growth of Li metal on the different surfaces, density functional theory (DFT) calculations were performed to analyze (i) the binding energies of Li and (ii) the surface energies of the (100) and (110) surfaces of Li and LiZn (Li:Zn = 1). In total, five surfaces were considered for the calculations (Li (100), Li-terminated LiZn (100), Zn-terminated LiZn (100), Li (110), and LiZn (110)), with

optimized structures as shown in Figure S8a. The calculations (Figure S8b) indicate that the alloy surfaces, including Li-terminated LiZn (100), Zn-terminated LiZn (100), and LiZn (110), show higher surface energies than the Li surfaces. These higher surface energy facets prefer to form three-dimensional structure as compared one-dimensional dendritic whiskers according to a surface nucleation and diffusion model.^{18,44} The binding energies of Li on the surfaces are then calculated to evaluate the thermodynamic affinity of the surfaces for Li atoms (Figure 6c), which is a key factor in determining the growth and agglomeration of Li during cycling. Interestingly, it can be seen that the LiZn alloy surface has stronger binding energies for Li at the Zn-related sites, suggesting that the LiZn alloy surface is favorable for the growth of Li due to its higher affinity for Li atoms. These computational results are in good agreement with our experimental observations.

4. CONCLUSIONS

In summary, a LiZn modified Li anode was prepared successfully by e-beam evaporation. The Zn sites of the alloy layer have a higher binding energy with Li, guiding ordered nucleation and growth of Li. Additionally, the electrochemically and structurally stable LiZn alloy surface modified layer helps to reduce the side reactions between the Li electrode and electrolyte and forms a stable SEI layer. As a result, when assembled as a symmetric cell, the alloy protects the Li metal anode to exhibits a longer cycling life (more than 1000 h at a current density of 2 mA cm⁻² with a total capacity of 1 mAh cm⁻²) with a lower deposition overpotential compared with the pure-Li metal anode. Moreover, when paired with a LFP cathode, the LiZn/Li//LFP full cell also delivers a higher CE (about 99.6%). The results show that the LiZn alloy modified layer can help to realize homogeneous deposition of Li to eventually reach a stable cycle life for robust Li metal batteries.

■ ASSOCIATED CONTENT

SI Supporting Information

The Supporting Information is available free of charge at <https://pubs.acs.org/doi/10.1021/acsami.0c21195>.

SEM images of Zn particles on Si substrate, XPS spectra, SEM images of Li deposition behavior on the LiZn/Li surface (with different thicknesses of LiZn), SEM images of Li deposition behavior on Li and the LiZn/Li surface after 100 cycles, additional electrochemical results (voltage profiles and EIS plots) and computational results (PDF)

■ AUTHOR INFORMATION

Corresponding Authors

Qingshui Xie – State Key Laboratory for Physical Chemistry of Solid Surfaces, Fujian Key Laboratory of Materials Genome, College of Materials, Xiamen University, Xiamen 361005, China; orcid.org/0000-0003-2105-6962; Email: xieqsh@xmu.edu.cn

Dong-Liang Peng – State Key Laboratory for Physical Chemistry of Solid Surfaces, Fujian Key Laboratory of Materials Genome, College of Materials, Xiamen University, Xiamen 361005, China; orcid.org/0000-0003-4155-4766; Email: dmpeng@xmu.edu.cn

C. Buddie Mullins – McKetta Department of Chemical Engineering, The University of Texas at Austin, Austin, Texas 78712, United States; Department of Chemistry, The

University of Texas at Austin, Austin, Texas 78712, United States; orcid.org/0000-0003-1030-4801; Email: mullins@che.utexas.edu

Authors

Qjulin Chen – McKetta Department of Chemical Engineering, The University of Texas at Austin, Austin, Texas 78712, United States; State Key Laboratory for Physical Chemistry of Solid Surfaces, Fujian Key Laboratory of Materials Genome, College of Materials, Xiamen University, Xiamen 361005, China

Hao Li – Department of Chemistry and Oden Institute for Computational Engineering and Sciences, The University of Texas at Austin, Austin, Texas 78712, United States; orcid.org/0000-0002-7577-1366

Melissa L. Meyerson – Department of Chemistry, The University of Texas at Austin, Austin, Texas 78712, United States

Rodrigo Rodriguez – McKetta Department of Chemical Engineering, The University of Texas at Austin, Austin, Texas 78712, United States

Kenta Kawashima – Department of Chemistry, The University of Texas at Austin, Austin, Texas 78712, United States; orcid.org/0000-0001-7318-6115

Jason A. Weeks – Department of Chemistry, The University of Texas at Austin, Austin, Texas 78712, United States

Hohyun Sun – McKetta Department of Chemical Engineering, The University of Texas at Austin, Austin, Texas 78712, United States

Jie Lin – State Key Laboratory for Physical Chemistry of Solid Surfaces, Fujian Key Laboratory of Materials Genome, College of Materials, Xiamen University, Xiamen 361005, China; orcid.org/0000-0002-1281-9713

Graeme Henkelman – Department of Chemistry and Oden Institute for Computational Engineering and Sciences, The University of Texas at Austin, Austin, Texas 78712, United States; orcid.org/0000-0002-0336-7153

Adam Heller – McKetta Department of Chemical Engineering, The University of Texas at Austin, Austin, Texas 78712, United States; orcid.org/0000-0003-0181-1246

Complete contact information is available at: <https://pubs.acs.org/doi/10.1021/acsami.0c21195>

Notes

The authors declare no competing financial interest.

■ ACKNOWLEDGMENTS

The authors gratefully acknowledge the Welch Foundation for their financial support of this work (F-1131 (A.H.), F-1436 (C.B.M.), and F-1841 (G.H.)). C.B.M. also acknowledges the U.S. National Science Foundation for support (Grant CBET-1603491). We also greatly appreciate the National Natural Science Foundation of China (Grants 51871188, 51701169, and 51931006), the National Key R&D Program of China (Grant 2016YFA0202602), and the Natural Science Foundation of Fujian Province of China (No. 2019J06003) for their generous support. Finally, we thank Dr. Hugo Celio, Dr. Raluca Gearba, and Mr. David K Gray for their contributions regarding XPS, FIB-SEM measurements, and crucible construction.

REFERENCES

- (1) Bruce, P. G.; Freunberger, S. A.; Hardwick, L. J.; Tarascon, J. M. Li-O₂ and Li-S batteries with high energy storage. *Nat. Mater.* **2012**, *11* (1), 19–29.
- (2) Yin, Y. X.; Xin, S.; Guo, Y. G.; Wan, L. J. Lithium-sulfur batteries: electrochemistry, materials, and prospects. *Angew. Chem., Int. Ed.* **2013**, *52* (50), 13186–200.
- (3) Peng, Z.; Freunberger, S. A.; Chen, Y.; Bruce, P. G. A reversible and higher-rate Li-O₂ battery. *Science* **2012**, *337* (6094), 563.
- (4) Shen, X.; Liu, H.; Cheng, X.-B.; Yan, C.; Huang, J.-Q. Beyond lithium ion batteries: higher energy density battery systems based on lithium metal anodes. *Energy Storage Mater.* **2018**, *12*, 161–175.
- (5) Xu, W.; Wang, J.; Ding, F.; Chen, X.; Nasybulin, E.; Zhang, Y.; Zhang, J.-G. Lithium metal anodes for rechargeable batteries. *Energy Environ. Sci.* **2014**, *7* (2), 513–537.
- (6) Lin, D.; Liu, Y.; Cui, Y. Reviving the lithium metal anode for high-energy batteries. *Nat. Nanotechnol.* **2017**, *12* (3), 194–206.
- (7) Liu, B.; Zhang, J.-G.; Xu, W. Advancing lithium metal batteries. *Joule* **2018**, *2* (5), 833–845.
- (8) Li, L.; Li, S.; Lu, Y. Suppression of dendritic lithium growth in lithium metal-based batteries. *Chem. Commun. (Cambridge, U. K.)* **2018**, *54* (50), 6648–6661.
- (9) Zhang, X.; Wang, A.; Liu, X.; Luo, J. Dendrites in lithium metal anodes: suppression, regulation, and elimination. *Acc. Chem. Res.* **2019**, *52* (11), 3223–3232.
- (10) Li, B.; Wang, Y.; Yang, S. A Material Perspective of Rechargeable Metallic Lithium Anodes. *Adv. Energy Mater.* **2018**, *8* (13), 1702296.
- (11) Zheng, H.; Zhang, Q.; Chen, Q.; Xu, W.; Xie, Q.; Cai, Y.; Ma, Y.; Qiao, Z.; Luo, Q.; Lin, J.; et al. 3D lithiophilic–lithiophobic–lithiophilic dual-gradient porous skeleton for highly stable lithium metal anode. *J. Mater. Chem. A* **2020**, *8* (1), 313–322.
- (12) Wang, H.; Liu, Y.; Li, Y.; Cui, Y. Lithium Metal Anode Materials Design: Interphase and Host. *Electrochem. Energy Rev.* **2019**, *2* (4), 509–517.
- (13) Zhang, H.; Eshetu, G. G.; Judez, X.; Li, C.; Rodriguez-Martinez, L. M.; Armand, M. Electrolyte Additives for Lithium Metal Anodes and Rechargeable Lithium Metal Batteries: Progress and Perspectives. *Angew. Chem., Int. Ed.* **2018**, *57* (46), 15002–15027.
- (14) Li, T.; Liu, H.; Shi, P.; Zhang, Q. Recent progress in carbon/lithium metal composite anode for safe lithium metal batteries. *Rare Met.* **2018**, *37* (6), 449–458.
- (15) Zhao, H.; Lei, D.; He, Y.-B.; Yuan, Y.; Yun, Q.; Ni, B.; Lv, W.; Li, B.; Yang, Q.-H.; Kang, F.; Lu, J. Compact 3D Copper with Uniform Porous Structure Derived by Electrochemical Dealloying as Dendrite-Free Lithium Metal Anode Current Collector. *Adv. Energy Mater.* **2018**, *8*, 1800266.
- (16) Ke, X.; Cheng, Y.; Liu, J.; Liu, L.; Wang, N.; Liu, J.; Zhi, C.; Shi, Z.; Guo, Z. Hierarchically Bicontinuous Porous Copper as Advanced 3D Skeleton for Stable Lithium Storage. *ACS Appl. Mater. Interfaces* **2018**, *10* (16), 13552–13561.
- (17) Yasin, G.; Arif, M.; Mehtab, T.; Lu, X.; Yu, D.; Muhammad, N.; Nazir, M. T.; Song, H. Understanding and suppression strategies toward stable Li metal anode for safe lithium batteries. *Energy Storage Mater.* **2020**, *25*, 644–678.
- (18) Cheng, X.-B.; Zhang, R.; Zhao, C.-Z.; Zhang, Q. Toward safe lithium metal anode in rechargeable batteries: a review. *Chem. Rev.* **2017**, *117* (15), 10403–10473.
- (19) Ely, D. R.; García, R. E. Heterogeneous nucleation and growth of lithium electrodeposits on negative electrodes. *J. Electrochem. Soc.* **2013**, *160* (4), A662.
- (20) Yan, K.; Lu, Z.; Lee, H.-W.; Xiong, F.; Hsu, P.-C.; Li, Y.; Zhao, J.; Chu, S.; Cui, Y. Selective deposition and stable encapsulation of lithium through heterogeneous seeded growth. *Nat. Energy* **2016**, *1* (3), 16010.
- (21) Pei, A.; Zheng, G.; Shi, F.; Li, Y.; Cui, Y. Nanoscale nucleation and growth of electrodeposited lithium metal. *Nano Lett.* **2017**, *17* (2), 1132–1139.
- (22) Zhang, F.; Shen, F.; Fan, Z.-Y.; Ji, X.; Zhao, B.; Sun, Z.-T.; Xuan, Y.-Y.; Han, X.-G. Ultrathin Al₂O₃-coated reduced graphene oxide membrane for stable lithium metal anode. *Rare Met.* **2018**, *37* (6), 510–519.
- (23) Zhang, C.; Lv, W.; Zhou, G.; Huang, Z.; Zhang, Y.; Lyu, R.; Wu, H.; Yun, Q.; Kang, F.; Yang, Q.-H. Vertically Aligned Lithiophilic CuO Nanosheets on a Cu Collector to Stabilize Lithium Deposition for Lithium Metal Batteries. *Adv. Energy Mater.* **2018**, *8* (21), 1703404.
- (24) Ke, X.; Liang, Y.; Ou, L.; Liu, H.; Chen, Y.; Wu, W.; Cheng, Y.; Guo, Z.; Lai, Y.; Liu, P.; Shi, Z. Surface engineering of commercial Ni foams for stable Li metal anodes. *Energy Storage Mater.* **2019**, *23*, 547–555.
- (25) Chen, Y.; Ke, X.; Cheng, Y.; Fan, M.; Wu, W.; Huang, X.; Liang, Y.; Zhong, Y.; Ao, Z.; Lai, Y.; Wang, G.; Shi, Z. Boosting the electrochemical performance of 3D composite lithium metal anodes through synergistic structure and interface engineering. *Energy Storage Mater.* **2020**, *26*, 56–64.
- (26) Cheng, Y.; Ke, X.; Shi, Z. Improving Li Plating Behaviors Through Cu–Sn Alloy-Coated Current Collector for Dendrite-Free Lithium Metal Anodes. *Acta Metall. Sin. (Engl. Lett.)* **2020**, DOI: 10.1007/s40195-020-01022-2.
- (27) Liang, Y.; Chen, Y.; Ke, X.; Zhang, Z.; Wu, W.; Lin, G.; Zhou, Z.; Shi, Z. Coupling of triporosity and strong Au–Li interaction to enable dendrite-free lithium plating/stripping for long-life lithium metal anodes. *J. Mater. Chem. A* **2020**, *8* (35), 18094–18105.
- (28) Cheng, Y.; Ke, X.; Chen, Y.; Huang, X.; Shi, Z.; Guo, Z. Lithiophobic-lithiophilic composite architecture through co-deposition technology toward high-performance lithium metal batteries. *Nano Energy* **2019**, *63*, 103854.
- (29) Ishikawa, M.; Morita, M.; Matsuda, Y. In situ scanning vibrating electrode technique for lithium metal anodes. *J. Power Sources* **1997**, *68* (2), 501–505.
- (30) Matsuda, Y. Behavior of lithium/electrolyte interface in organic solutions. *J. Power Sources* **1993**, *43* (1–3), 1–7.
- (31) Jin, C.; Sheng, O.; Lu, Y.; Luo, J.; Yuan, H.; Zhang, W.; Huang, H.; Gan, Y.; Xia, Y.; Liang, C.; Zhang, J.; Tao, X. Metal oxide nanoparticles induced step-edge nucleation of stable Li metal anode working under an ultrahigh current density of 15 mA cm⁻². *Nano Energy* **2018**, *45*, 203–209.
- (32) Perdew, J. P.; Burke, K.; Ernzerhof, M. Generalized gradient approximation made simple. *Phys. Rev. Lett.* **1996**, *77* (18), 3865.
- (33) Blöchl, P. E. Projector augmented-wave method. *Phys. Rev. B: Condens. Matter Mater. Phys.* **1994**, *50* (24), 17953.
- (34) Kohn, W.; Sham, L. J. Self-consistent equations including exchange and correlation effects. *Phys. Rev.* **1965**, *140* (4A), A1133.
- (35) Wood, K. N.; Teeter, G. XPS on Li-Battery-Related Compounds: Analysis of Inorganic SEI Phases and a Methodology for Charge Correction. *ACS Applied Energy Materials* **2018**, *1* (9), 4493–4504.
- (36) Ahmad, M.; Yingying, S.; Sun, H.; Shen, W.; Zhu, J. SnO₂/ZnO composite structure for the lithium-ion battery electrode. *J. Solid State Chem.* **2012**, *196*, 326–331.
- (37) Ahn, J.; Park, J.; Kim, J. Y.; Yoon, S.; Lee, Y. M.; Hong, S.; Lee, Y.-G.; Phatak, C.; Cho, K. Y. Insights into Lithium Surface: Stable Cycling by Controlled 10 μm Deep Surface Relief, Reinterpreting the Natural Surface Defect on Lithium Metal Anode. *ACS Applied Energy Materials* **2019**, *2* (8), 5656–5664.
- (38) Wang, D.; Zhang, W.; Zheng, W.; Cui, X.; Rojo, T.; Zhang, Q. Towards High-Safe Lithium Metal Anodes: Suppressing Lithium Dendrites via Tuning Surface Energy. *Adv. Sci. (Weinh)* **2017**, *4* (1), 1600168.
- (39) Wu, S.; Zhang, Z.; Lan, M.; Yang, S.; Cheng, J.; Cai, J.; Shen, J.; Zhu, Y.; Zhang, K.; Zhang, W. Lithiophilic Cu–CuO–Ni Hybrid Structure: Advanced Current Collectors Toward Stable Lithium Metal Anodes. *Adv. Mater.* **2018**, *30* (9), 1705830.
- (40) Wang, D.; Luan, C.; Zhang, W.; Liu, X.; Sun, L.; Liang, Q.; Qin, T.; Zhao, Z.; Zhou, Y.; Wang, P.; Zheng, W. Zipper-inspired SEI film for remarkably enhancing the stability of Li metal anode via

nucleation barriers controlled weaving of lithium pits. *Adv. Energy Mater.* **2018**, *8* (21), 1800650.

(41) Chen, K.-H.; Wood, K. N.; Kazyak, E.; LePage, W. S.; Davis, A. L.; Sanchez, A. J.; Dasgupta, N. P. Dead lithium: mass transport effects on voltage, capacity, and failure of lithium metal anodes. *J. Mater. Chem. A* **2017**, *5* (23), 11671–11681.

(42) Li, N. W.; Yin, Y. X.; Yang, C. P.; Guo, Y. G. An artificial solid electrolyte interphase layer for stable lithium metal anodes. *Adv. Mater.* **2016**, *28* (9), 1853–1858.

(43) Liu, Y. Y.; Lin, D. C.; Yuen, P. Y.; Liu, K.; Xie, J.; Dauskardt, R. H.; Cui, Y. An Artificial Solid Electrolyte Interphase with High Li-Ion Conductivity, Mechanical Strength, and Flexibility for Stable Lithium Metal Anodes. *Adv. Mater.* **2017**, *29* (10), 1605531.

(44) Ling, C.; Banerjee, D.; Matsui, M. Study of the electrochemical deposition of Mg in the atomic level: why it prefers the non-dendritic morphology. *Electrochim. Acta* **2012**, *76*, 270–274.